Supplementary Materials: The Influence of Mechanical Deformations on Surface Force Measurements

Romain Lhermerout

1. Models of contact mechanics

In this section, we briefly recall the hypotheses and consequences associated to the different models of contact mechanics, that are used to analyze the measurements (reviews can be found in [1–4]). All the models presented here rely on a common set of hypotheses or approximations. The two solid bodies in contact are supposed (i) semi-infinite, (ii) composed of linear (no plasticity) homogeneous (no stack of layers) isotropic (not crystalline) and purely elastic (no viscosity) materials, (iii) with perfectly smooth and frictionless surfaces and (iv) in a regime where the contact radius is much smaller than their radius of curvature: $a \ll R$. These models differ in the way adhesion is taken into account. In the following, we consider the simple geometry of two cylinders of same radius of curvature R and material that are crossed at 90 degrees (or equivalently a sphere of radius of curvature R and a plane of same material), with the top solid controlled in position and the bottom solid mounted on a spring of stiffness k (see sketch in Figure 1b).

In Hertz model [5], it is hypothesized that there are no attractive forces between the surfaces (hard wall interaction, acting inside the contact area only). The normal force (or load) F, contact radius a and indentation δ (defined positive for compression and negative for dilatation) are related by:

$$\begin{cases} F = \dfrac{Ka^3}{R} \\ \delta = \dfrac{a^2}{R} \end{cases}, \tag{1}$$

where $K = \frac{2}{3}\frac{E}{1-\nu^2}$ is the elastic modulus, with E the Young's modulus and ν the Poisson's ratio. At lateral scale $|x| \ll R$, the distance z between the surfaces is given by:

$$z = \begin{cases} \dfrac{a^2}{\pi R}\left[\sqrt{\left(\dfrac{x}{a}\right)^2 - 1} + \left(\left(\dfrac{x}{a}\right)^2 - 2\right)\arctan\sqrt{\left(\dfrac{x}{a}\right)^2 - 1}\right] & \text{for } |x| \geq a \\ 0 & \text{for } |x| < a \end{cases}. \tag{2}$$

When moving up the top solid, the surfaces separate at $F_s = 0$, $a_s = 0$, $\delta_s = 0$, with no jump-out.

In Derjaguin-Muller-Toporov (DMT) model [6], attractive forces of finite range are added (sticky hard wall interaction, acting inside the contact area and in a ring-shaped zone outside the contact area), but adhesion is assumed not to deform the surfaces, leading to a discontinuity of the normal stress at the edge of the contact area. The normal force (or load) F, contact radius a and indentation δ are related by:

$$\begin{cases} F = \dfrac{Ka^3}{R} - 2\pi RW \\ \delta = \dfrac{a^2}{R} \end{cases}, \tag{3}$$

where W is the adhesion energy (per unit area, taken positive) and the deformation profile $z(x)$ is the same than in the Hertz model. When moving up the top solid, the surfaces separate at $F_s = -2\pi RW$, $a_s = 0$, $\delta_s = 0$, with a jump-out over a distance $2\pi RW/k$ due to the spring instability. Note that the relationship between the jump-out force and the adhesion energy coincides with the one given by the Derjaguin approximation [1,7], because the

surfaces are not deformed at the point of minimum force in the DMT model and supposed undeformable in the context of the Derjaguin approximation.

In Johnson-Kendall-Roberts (JKR) model [8], attractive forces of zero range are added (Baxter i.e., infinitely short range square interaction, acting only inside the contact area) and adhesion can deform the surfaces, leading to a divergence of the normal stress at the edge of the contact area. The normal force (or load) F, contact radius a and indentation δ are related by:

$$\begin{cases} F = \left[\sqrt{\frac{Ka^3}{R}} - \sqrt{\frac{3}{2}\pi RW}\right]^2 - \frac{3}{2}\pi RW \\ \delta = \frac{a^2}{R}\left[1 - \frac{4}{3}\left(\frac{a_s}{a}\right)^{3/2}\right] \end{cases}, \tag{4}$$

with $a_s = \left(\frac{3\pi R^2 W}{2K}\right)^{1/3}$. At lateral scale $|x| \ll R$, the distance z between the surfaces is given by:

$$z = \begin{cases} \frac{a^2}{\pi R}\left[\sqrt{\left(\frac{x}{a}\right)^2 - 1} + \left(\left(\frac{x}{a}\right)^2 - 2 + \frac{8}{3}\left(\frac{a_s}{a}\right)^{3/2}\right)\arctan\sqrt{\left(\frac{x}{a}\right)^2 - 1}\right] & \text{for } |x| \geq a \\ 0 & \text{for } |x| < a \end{cases}. \tag{5}$$

When moving up the top solid, the surfaces separate at the point where $\frac{dF}{d\delta} = -k$. If the spring constant is low enough, this condition can be approximated by $\frac{dF}{d\delta} = 0$ and the surfaces separate at $F_s = -\frac{3}{2}\pi RW$, $a_s = \left(\frac{3\pi R^2 W}{2K}\right)^{1/3}$, $\delta_s = -\left(\frac{\pi^2 RW^2}{12K^2}\right)^{1/3}$, with a jump-out over a distance $\frac{3}{2}\pi RW/k$.

In Maugis model [3], attractive forces of finite range d are added (Dugdale i.e., square-well interaction, acting inside the contact area and in a ring-shaped zone outside the contact area) and adhesion can deform the surfaces, leading to a normal stress that presents no singularity at the edge of the contact area. The normal force (or load) F, contact radius a and indentation δ are related by implicit equations, together with a dimensionless parameter here denoted as Ma:

$$\mathrm{Ma} = \left(\frac{8RW^2}{\pi K^2 d^3}\right)^{1/3}. \tag{6}$$

Physically, Ma is the ratio between the elastic indentation due to adhesion and the range of the attractive forces themselves. The three previous models are special cases of Maugis model: Hertz limit corresponds to $\mathrm{Ma} = 0$, DMT applies for $\mathrm{Ma} \ll 1$ and JKR is recovered for $\mathrm{Ma} \gg 1$. In the transition regime $\mathrm{Ma} \sim 1$, none of the DMT and JKR models are valid and the implicit equations from Maugis model have to be used to describe the contact mechanics.

2. Method for the determination of surface deformations

In this section, we explain in details the procedure of analysis of the FECO to deduce the apical distance D and the geometry of the surfaces, i.e., the radius of curvature R and the contact radius a (defined in Figure 1b). In general, the glue used to prepare the surfaces is heterogeneous in thickness, leading to a local radius of curvature of mica that is different from the radius of curvature of the supporting glass lens and differs from one surface to the other (by typically $\sim 10\%$); therefore crossing the two cylinders at right angle results in a contact zone of elliptic symmetry. During the experiments, we observe the FECO along only one direction x parallel to the axis of symmetry of one lens (typical FECO images for N_2 and $[C_4C_1Pyrr][NTf_2]$ cases shown in Figure 2a,c), that is why to interpret the data we approximate the contact zone as a disk, i.e., we suppose that the surface deformation is the same in the perpendicular direction y.

In (wavelength λ)-(lateral distance x) space first, we measure the shape $\lambda_p(x)$ of fringe of odd order p. For each line, the fringe position is detected by calculating the center of mass of the doublet (due to mica birefringence) after applying a threshold on the image (when the intensity is smaller than the threshold, it is set equal to the threshold). The threshold is chosen just above the intensity fluctuations of the background, to reduce the noise on the signal. Provided that the mica thickness is constant and known, the separation profile between the mica surfaces $z(x)$ can then be deduced (typical profiles for N_2 and $[C_4C_1Pyrr][NTf_2]$ cases shown in Figure 2b,d) [9]. The separation profile is measured up to a maximum scale $z_{max} \sim 50$ nm $\ll R \sim 1$ cm, that is why the undeformed shape (when the surfaces are far from contact), circular in theory, is here observed locally and very well described by a parabola. There, a fitting procedure is used to extract D, R and a. On one hand, a parabolic fit is done at small scale close to the apex (green curve in Figure 2b,d), with 3 free parameters, giving the apical distance D (negative in the present cases shown in the Figures, as explained in details in the main text). On the other hand, R and a are obtained with different methods, depending whether the solid surfaces are separated by N_2 or by $[C_4C_1Pyrr][NTf_2]$.

In the case of $[C_4C_1Pyrr][NTf_2]$, the mechanical deformations are limited to a scale $z \ll z_{max}$ and the separation profile matches the undeformed shape at large measurable distances $z \sim z_{max}$. A second parabolic fit is done at large scale only (blue curve in Figure 2d), with a function of the form:

$$z = z_0 + \frac{(x - x_0)^2}{2R}, \tag{7}$$

where x_0 and z_0 are 2 free parameters controlling the position of the parabola and $R = 0.92 \pm 0.01$ cm is the radius of curvature that is adjusted using one image when the surfaces are far from contact and then kept fixed. By definition, the contact radius is the lateral distance $|x - x_0|$ at which the extrapolated undeformed profile crosses the contact plane at $z = D$ and is simply given by $a = \sqrt{2R(D - z_0)}$. To do this parabolic fit at large scale only, the points associated to values $|x - x_0| < a$ are excluded from the fit and the fitting procedure is repeated iteratively: on first iteration no point is excluded and a value a_1 is deduced, on second iteration a_1 is used to exclude some points from the fit and a_2 is deduced, etc. In practice, 3 iterations are enough for the value of a to converge, as additional iterations lead to insensitive changes.

In the case of N_2, the mechanical deformations turn to be present at all measurable scales $z \leq z_{max}$ and the undeformed region of the profile cannot be observed. That is why the general definition of the contact radius a cannot be used and a model is needed to fit the deformation. A fit of the separation profile is done at all measurable scales (blue curve in Figure 2b), with a function derived from the JKR model (Equation (5)):

$$z = \begin{cases} D + \dfrac{a^2}{\pi R}\left[\sqrt{\left(\dfrac{x - x_0}{a}\right)^2 - 1} + \left(\left(\dfrac{x - x_0}{a}\right)^2 - 2 + \dfrac{8}{3}\left(\dfrac{a_s}{a}\right)^{3/2}\right) \arctan\sqrt{\left(\dfrac{x - x_0}{a}\right)^2 - 1}\right] \\ \quad \text{for } |x - x_0| \geq a \\ D \quad \text{for } |x - x_0| < a \end{cases}, \tag{8}$$

where the contact radius a and the center of the contact zone x_0 are 2 free parameters, the apical distance D is known from the small scale parabolic fit, the radius of curvature $R = 0.92 \pm 0.01$ cm is adjusted using one image when the surfaces are far from contact and then kept fixed and the contact radius at the jump-out point $a_s = 10.23$ μm is adjusted using the image just before the jump-out of the surfaces and then kept fixed (see the corresponding FECO image and separation profile in Figure S1a and Figure S1b).

It is clearly visible in Figure 2b that the JKR model doesn't fit well the deformed profile at the edge of the contact zone, as it predicts a corner at right angle while the data exhibit a much smoother profile. The angular shape given by the JKR model is in fact non-physical and is associated with the divergence of the normal stress at the edge of the contact zone.

This discrepancy was already mentioned in the seminal work by Horn, Israelachvili and Fribac [2], where the smooth measured profile was thought to be dominated by the flexural stiffness of the mica layer. This non perfect flattening is therefore well known, but is highlighted here compared to previous studies (see for example [10]) because of the use of a substantially thicker mica and of a sub-pixel-detection technique to characterize the fringe profile. Nonetheless, we keep the JKR fit as a first order determination of the contact radius and we see in the main text that this provides a variation of the contact radius with the force that is consistently well described by the JKR model and an effective elastic modulus describing the layered solid surfaces.

In order to obtain a reliable characterization of the geometry, note that all the images had to be rotated by the same angle (of the order of the degree) before this analysis, due to the fact that the camera is not perfectly aligned with the entrance slit of the spectrometer and so the raw image is not ideally symmetric. One image, corresponding to a situation when the surfaces are far from contact, is rotated by a given angle and the separation profile is fitted at all scales with a parabola. The values of rotation angles are scanned and the optimum angle corresponds to the fit associated with the minimum sum of squared residuals.

Finally, a is measured with a precision of 0.03 μm given by the standard deviation of the signal and an accuracy of 1 μm due to the uncertainty on the value of R (mainly caused by the fact that the separation profile is observed up to a maximum scale $z_{\max} \sim 50$ nm $\ll R \sim 1$ cm). This means that this method doesn't provide reliable values of a when $a \lesssim 1$ μm, which is typically the case for $[C_4C_1Pyrr][NTf_2]$ under low loads.

In the literature, the measured force F is generally rescaled by the radius of curvature R to compute an equivalent surface energy F/R, considering that mechanical deformations are negligible and that the Derjaguin approximation applies. In the opposite case when the surfaces are strongly flattened, it is reasonable to assume that the total force F is mainly due to the interaction in the flattened region and so to rescale it by the contact area πa^2 to compute the mean local pressure $F/(\pi a^2)$. In this study, we explore a broad range of situations from non measurable deformation to strong deformations, that is why we have chosen to simply use the force F without any rescaling in the plots.

References

1. Israelachvili, J.N. *Intermolecular and Surface Forces*, Third Edition; Academic Press: San Diego, CA, USA, 2011. doi:10.1016/B978-0-12-375182-9.10010-7.
2. Horn, R.G.; Israelachvili, J.N.; Pribac, F. Measurement of the Deformation and Adhesion of Solids in Contact. *J. Colloid Interface Sci.* **1987**, *115*, 480–492. doi:10.1016/0021-9797(87)90065-8.
3. Maugis, D. Adhesion of spheres: The JKR-DMT transition using a dugdale model. *J. Colloid Interface Sci.* **1992**, *150*, 243–269. doi:10.1016/0021-9797(92)90285-T.
4. Grierson, D.S.; Flater, E.E.; Carpick, R.W. Accounting for the JKR-DMT transition in adhesion and friction measurements with atomic force microscopy. *J. Adhes. Sci. Technol.* **2005**, *19*, 291–311. doi:10.1163/1568561054352685.
5. Hertz, H. Ueber die Berührung fester elastischer Körper. *J. für die Reine und Angew. Math.* **1882**, *19*, p. 156. doi:10.1515/crll.1882.92.156.
6. Derjaguin, B.V.; Muller, V.M.; Toporov, Y.P. Effect of Contact Deformations on the Adhesion of Particles. *J. Colloid Interface Sci.* **1975**, *53*, 314–326. doi:10.1016/0021-9797(75)90018-1.
7. Derjaguin, B. Untersuchungen über die Reibung und Adhäsion, IV. *Kolloid-Zeitschrift* **1934**, *69*, 155–164. doi:10.1007/BF01433225.
8. Johnson, K.L.; Kendall, K.; Roberts, A.D.; Tabor, D. Surface energy and the contact of elastic solids. *Proc. R. Soc. A* **1971**, *324*, 301–313. doi:10.1098/rspa.1971.0141.
9. Israelachvili, J.N. Thin Film Studies Using Multiple-Beam Interferometry. *J. Colloid Interface Sci.* **1973**, *44*, 259–272. doi:10.1016/0021-9797(73)90218-X.
10. Israelachvili, J.N.; Perez, E.; Tandon, R.K. On the adhesion force between deformable solids. *J. Colloid Interface Sci.* **1980**, *78*, 260–261. doi:10.1016/0021-9797(80)90520-2.

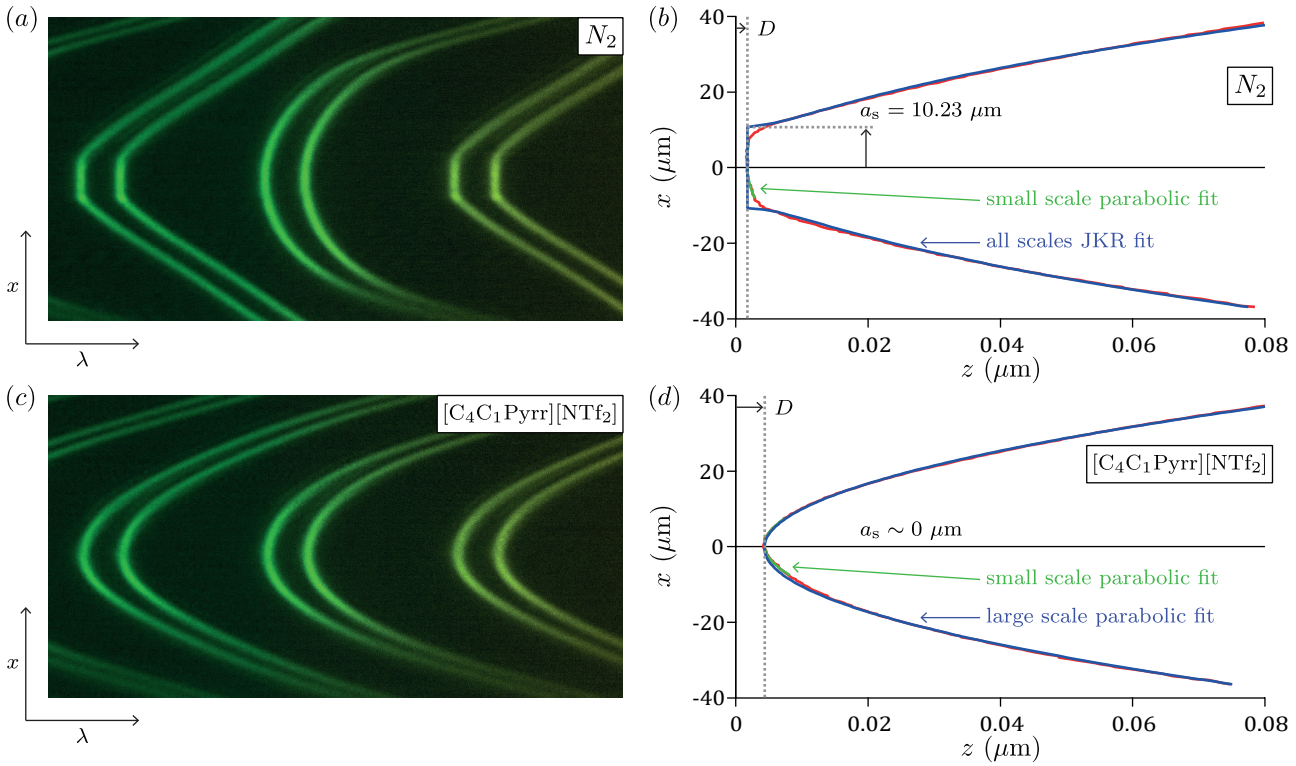

Figure S1. (a) Picture of the FECO when the two solid surfaces are in contact across N_2, observed in (wavelength λ)-(lateral distance x) space. (b) Corresponding profile of the distance z between the surfaces along the lateral coordinate x (in red). A parabolic fit at small scale close to the apex (in green) allows to measure the apical distance D, while a fit with the JKR profile (Equation (5) in main text) at all measured scales (in blue) is used to extract the contact radius a. (c) Picture of the FECO when the two solid surfaces are in contact across $[C_4C_1Pyrr][NTf_2]$, observed in (wavelength λ)-(lateral distance x) space. (d) Corresponding profile of the distance z between the surfaces along the lateral coordinate x (in red). A parabolic fit at small scale close to the apex (in green) allows to measure the apical distance D, while a parabolic fit at large scale (in blue) is used to extract the contact radius a. The two particular cases shown here correspond to the jump-out points reached in Figure 3 in main text.

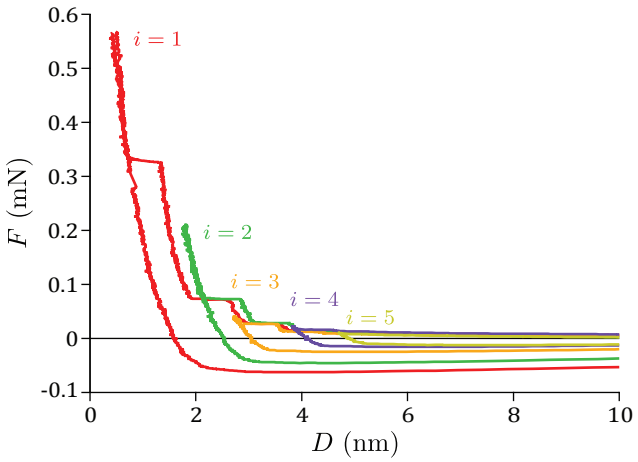

Figure S2. Force profile measured with $[C_4C_1Pyrr][NTf_2]$ between mica surfaces when approaching or retracting the top surface with the piezoelectric tube at $v = 0.5$ nm/s, showing structuring with 5 distinguishable layers labeled by i. The different colors stand for approach up to a given layer and retraction from this layer: $i = 1$ in red, $i = 2$ in green, $i = 3$ in orange, $i = 4$ in purple and $i = 5$ in yellow.

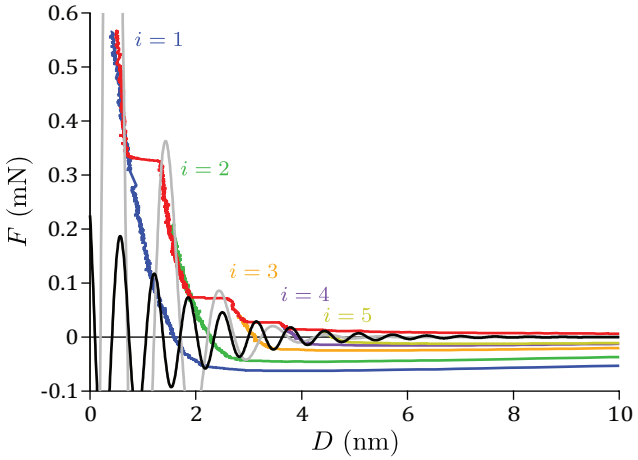

Figure S3. Force profile measured with $[C_4C_1Pyrr][NTf_2]$ between mica surfaces when approaching or retracting the top surface with the piezoelectric tube at $v = 0.5$ nm/s, showing structuring with 5 distinguishable layers labeled by i. For clarity, only the full approach is shown (in red), together with retractions from layers $i = 1$ (in blue), $i = 2$ (in green), $i = 3$ (in orange), $i = 4$ (in purple), $i = 5$ (in yellow). The gray curve is an exponentially decaying harmonic oscillation (Equation (10) in main text) with parameters $F_0 = F_0^{\max}$, $D_0 = D_0^{\max}$, $\zeta = \zeta^{\max}$ and $\lambda = \lambda^{\max}$ obtained from the fits of the points of maximum force. The black curve is an exponentially decaying harmonic oscillation (Equation (10) in main text) with parameters $F_0 = F_0^{\min}$, $D_0 = D_0^{\min}$, $\zeta = \zeta^{\min}$ and $\lambda = \lambda^{\min}$ obtained from the fits of the points of minimum force (see Equations (11) and (12) and Figure 4b,c in main text).